RSC Advances

PAPER

View Article Online
View Journal | View Issue

Cite this: *RSC Adv.*, 2023, **13**, 3255

Strong metal–support interactions between atomically dispersed Ru and CrO_x for improved durability of chlorobenzene oxidation†

Xi Chen, Ziliang Jia, Zhihong Liu, Xiaoyan Wang and Meisheng Liang *

In this work, two single-atom catalysts (SACs) with atomically dispersed RuO_2 supported on CrO_x were successfully synthesized with a simple reduction strategy for the efficient catalytic oxidation of chlorobenzene (CB). With characterizations like Cs-corrected STEM, XPS, H_2-TPR, and O_2-TPD, the structure–activity relationship is addressed. The noble metal precursor Ru^{3+} was anchored with different oxygen species and exposed facets based on the physicochemical properties of catalyst supports. Based on the analysis results, the Ru^{3+} precursor could be mainly anchored into the surface lattice oxygen of Cr_2O_3-M over high-index facets (223) and adsorbed oxygen of Cr_2O_3-P over low-index facets (104), where the precursor Ru^{3+} was all oxidized to RuO_2 when being anchored with the oxygen species of Cr_2O_3-M and Cr_2O_3-P, respectively according to XPS analysis. There is a stronger metal–support interaction (SMSI) between Ru ions and the surface lattice oxygen of Cr_2O_3-M, according to H_2-TPR and O_2-TPD characterizations. Further, the catalytic performance for CB combustion at a high space velocity of 120 000 mL (g^{-1} h^{-1}) was tested, and $1RuCr_2O_3$-M performed better than $1RuCr_2O_3$-P in both durability and activity. This could be attributed to the SMSI between single-atom Ru and the lattice oxygen of the $1RuCr_2O_3$-M catalyst and the abundant active sites from the exposed high-index facets. The study provided a novel synthesis strategy for Ru-based SACs with SMSI effect, and the good durability of the catalyst ($1RuCr_2O_3$-M) extended the great potential for practical application.

Received 1st December 2022
Accepted 8th January 2023

DOI: 10.1039/d2ra07650k

rsc.li/rsc-advances

1 Introduction

Chlorinated volatile organic compounds (CVOCs) are attractive due to their similar molecular structure to polychlorinated dibenzo-*p*-dioxins (PCDDs) and dibenzofurans (PCDFs).[1] Because of their stable chemical and degradation-resistant properties, there are high quantities of CVOCs in the environment, *e.g.*, coming from waste incineration flue gas of metallurgical industries and consumption of fossil energy, and bring about severe environmental issues.[2,3] They cause multiple health problems for humans and animals, such as cancer and aberration.[4,5] Stringent environmental regulations have been adopted in many countries to prevent or remove the emission of these hazardous compounds.[6] In laboratory research, chlorobenzene (CB) is often used as the indicator to evaluate the catalytic activity of catalysts for the oxidation of dioxins.[7] Catalytic combustion is one promising technology to oxidize CB to harmless or low toxicity compounds at low temperatures, and a lower concentration of contaminants can be eliminated compared with other technologies.[8] The development of catalysts with high activity and stability is a desired factor for the removal of CB by catalytic combustion technology.[9]

Research has focused on metal oxide and noble metal catalysts.[10] Nobel metal catalysts have attracted attention due to their good catalytic activities for heterogeneous catalysis[11] at lower temperatures.[12] Yet, some intrinsic properties of noble metals inhibit practical application, such as cost, particle agglomeration, and the fact they can be poisoned by organochlorine adsorption.[13] To overcome these disadvantages, the preparation of SACs (single atom catalyst) may be useful. In previous studies, the SACs have displayed superiorities in CO oxidation[14] photochemical water splitting, sensing,[15] *etc.* The limited examples of oxidation of VOCs have provided the need for the development of SACs in this field.[16] It is well known that ruthenium is the cheapest among the precious metal series (including Pt, Pd, Au, and Ru). We used $RuCl_3$ as the noble metal precursor, with the single-atom dispersed Ru maximizing the utilization efficiency of precious metals in the catalytic process, which reduced the cost of catalyst preparation. Cr_2O_3 was selected as the catalyst supports because of its thermostability and poisoning resistance during organic oxidation reactions.[17] It can be deduced from our previous studies that

College of Environmental Science and Engineering, Taiyuan University of Technology, Taiyuan, China. E-mail: liangmeisheng@tyut.edu.cn

† Electronic supplementary information (ESI) available: (1) EDS analysis of $1Ru/Cr_2O_3$-P and $1Ru/Cr_2O_3$-M, (2) Nitrogen adsorption–desorption isotherms and pore size distributions of $1Ru/Cr_2O_3$-P and $1Ru/Cr_2O_3$-M, and (3) CB conversion and CO_2 mineralization rate of samples with CB concentration = 1000 ppm and SV = 60 000 mL (g^{-1} h^{-1}). See DOI: https://doi.org/10.1039/d2ra07650k

different synthesis strategies often lead to different physicochemical properties of the same catalyst supports.[18,19]

Atomically dispersed catalyst $1RuCr_2O_3$-P and $1RuCr_2O_3$-M composites with similar amounts of Ru (~0.9 wt% loading) were successfully prepared through a simple reduction method, where Cr_2O_3-P was obtained by precipitation and Cr_2O_3-M was derived from the pyrolysis of a MOF-template as in a previous study.[18] The results indicated that $1RuCr_2O_3$-M showed the best catalytic activity and promoted stability. Calcination temperatures, amounts (measured by ICP-OES), and morphology (observed by Cs-corrected STEM) indicate that the better performance of $1RuCr_2O_3$-M on CB oxidation could result from the stable Ru–O structure with a strong metal–support interaction (SMSI) effect. This can effectively restrain the mutual contact of noble metals and inhibit the aggregation and migration of single atoms.

We examined how catalytic activities influenced by the interaction between these two components (Ru and O). With several characterizations, including XPS, H_2-TPR, and O_2-TPD, we found that Ru^{3+} were anchored into different crystals of catalyst supports. This resulted in a different catalytic performance of CB oxidation, where Ru^{3+} could be mainly anchored into the surface lattice oxygen of Cr_2O_3-M over the high-index (223) facets and adsorbed oxygen of Cr_2O_3-P over low-index (104) facets. Then atomically dispersed RuO_2 was formed on the Cr_2O_3-M and Cr_2O_3-P supports after the oxidation of Ru^{3+}. The better durability performance for chlorobenzene oxidation is mainly due to the SMSI effect of Ru ions and lattice oxygen species.

2 Experimental section

2.1 Chemicals and materials

Analytical reagents were used without further purification. $NaBH_4$, HF, NH_4OH (25–28%), Cr $(NO_3)_3 \cdot 9H_2O$, and chlorobenzene were obtained from Sinopharm Chemical Reagent Co., Ltd (Shanghai, China). $RuCl_3$ was purchased from Shaanxi Kaida Chemical Engineering Co., Ltd (Shanghai, China); 1,4-dicarboxybenzene was obtained from Aladin (Shanghai, China).

2.2 Preparation of Cr_2O_3-M and $1RuCr_2O_3$-M

The catalyst precursor MIL-101-Cr and its derived product Cr_2O_3-M were prepared according to a previous study.[19] The catalyst $1RuCr_2O_3$-M (Ru = 0.88 wt%, according to the results of ICP-OES) was synthesized *via* a simple reduction method using $NaBH_4$ for the reduction of Ru^{3+}. Precisely, a gram of Cr_2O_3-M was homogenously dispersed in DI water by ultrasonic dispersion, then the desired amount of $RuCl_3$ solution with 1 wt% of Ru content was dropwise added into the suspension under vigorous stirring. Then a certain amount of $NaBH_4$ aqueous solution was added to the resulting mixture after stirring for 1 h. The sample was collected by filtration and then dried at 120 °C for several hours, and finally calcined at 500 °C under air for 2 h.

2.3 Preparation of Cr_2O_3-P and $1RuCr_2O_3$-P

Cr_2O_3-P was prepared by a precipitation method, where $Cr(NO_3)_3 \cdot 9H_2O$ and NH_4OH were used as the precursor and precipitant, respectively. Typically, 2.0 g of $Cr(NO_3)_3 \cdot 9H_2O$ was dissolved in 50 mL of DI water as chromium ions sources; 2.3 g of NH_4OH was added into 50 mL of DI water to obtain the uniform ammonia solution, and then was added dropwise into the solution of $Cr(NO_3)_3 \cdot 9H_2O$. The mixture was stirred overnight on a magnetic stirrer and aged for about 2 h. The solid was isolated by decantation and washed with water several times until the pH value of the supernatant was close to neutral. The obtained product was dried at 120 °C and calcined at 500 °C for 2 h. The synthesis of $1RuCr_2O_3$-P was similar to that of $1RuCr_2O_3$-M. The amount of supported Ru was confirmed by regional energy spectrum analysis (shown in Fig. S1†), which achieved a similar value to that of ICP-OES (Ru = 0.91 wt%).

2.4 Catalytic tests for chlorobenzene oxidation

Catalytic performance was tested in fixed-bed equipment, in which 66 mg of catalysts (40–60 mesh) were packed into a quartz tube with a 6 mm inner diameter. Each end of the catalyst bed was blocked by quartz sands and wool to stabilize the gas flow and to protect the catalysts from being blown away. CB (1000 ppm) with 66 mL min^{-1} or 132 mL min^{-1} of airflow passed through the catalyst bed to give the space velocity (SV) of 60 000 mL (g^{-1} h^{-1}) and 120 000 mL (g^{-1} h^{-1}). CB gas was produced through continuous gas bubbling of air into a liquid CB saturator, where the concentrations of CB were related to the environment temperature controlled by a cooling circulation system. Reaction temperatures were set in the range of 200–500 °C, which were monitored at the bottom of the catalyst bed using a thermocouple. The gas flow passed through the catalysts from top to bottom. To more accurately reflect the activities of catalysts, each temperature point was extended to as long as 40 min.

The effect of water was achieved by bubbling air (120 000 mL g^{-1} h^{-1}) through the water at 28 °C to yield a relative humidity of approximately 5%. To ensure the moist air could fully pass through the catalysts rather than condense on the inner walls of pipes, they were highly insulated to keep the temperature at ~110 °C in reactions. The concentrations of CB and CO_2 from the inlet and outlet were analyzed online by a gas chromatograph (GC) with a flame ionization detector and a thermal conductivity detector (TCD), respectively. CB conversion was achieved according to the formula $100\% \times (C_{in} - C_{out})/C_{in}$, where C_{in} and C_{out} indicate the CB concentrations of inlet and outlet gases, respectively. And the mineralization rate in CB combustion was calculated as $100\% \times M(CO_2)/M(CO_2)_t$, where $M(CO_2)$ is the concentration of CO_2 generated during the reaction at the corresponding temperature and $M(CO_2)_t$ signifies the calculated concentration of CO_2 from the full decomposition of CB in theory.

2.5 Durability measurements

Durability tests were performed on $1RuCr_2O_3$-M and $1RuCr_2O_3$-P under both dry and humid conditions, where 120 000 mL (g^{-1}

h^{-1}) and 305 °C were selected as the space velocity and test temperature.

2.6 Characterizations

The elemental content of Ru was measured using inductively coupled plasma-optical emission spectroscopy (ICP-OES). The phase compositions and chemical bonding states of catalysts were characterized by power X-ray diffraction (XRD, Panalytical X'Pert Pro; Holland) and Raman spectra (HJY, France), respectively. The BET surface areas, structure compositions, pore size distributions, *etc.* were measured using an automated physical adsorption apparatus (Quantachrome; America). The morphologies, crystal structures, and element distributions of prepared catalysts were observed by transmission electronic microscopy (TEM, JEM 2100F; Japan). Spherical aberration-corrected transmission electron microscopy (JEM ARM 200F) was conducted for the observation of the distribution of noble metals supported. H_2 temperature-programmed reduction (H_2-TPR) was determined by a chemical sorption instrument (Quantachrome; America), which was also used for oxygen temperature-programmed desorption analysis (O_2-TPD) as well. Ammonia temperature-programmed characterization (NH_3-TPD) was conducted by the above chemical sorption analyzer connecting a mass spectrum (Quantachrome; America) for the detection of desorbed NH_3 signals. X-ray photoelectron spectroscopy (XPS) was performed using a PerkinElmer model PHI 5600 model system equipped with an Al Kα X-ray source ($h\nu$ = 1486.6 eV). All the peaks corresponding to certain binding energies were calibrated according to the signal of carbon at a binding energy of 284.8 eV, and the curves were fitted carefully. *In situ* DRIFTS (Thermo Fisher; America) were conducted for mechanistic assessment of CB oxidation under N_2 and air atmospheric pressure.

3 Results and discussion

3.1 Structural analysis

As seen in Fig. 1(a), the XRD results indicate that there is little difference in the catalyst peaks with or without Ru loading, where no new peaks corresponding to metallic Ru or oxidation state of Ru (RuO_x) can be observed in Ru-based catalysts. The only difference is that the intensity of the XRD pattern for 1$RuCr_2O_3$-M is weaker than that of Cr_2O_3-M whereas it is so close for 1$RuCr_2O_3$-P and Cr_2O_3-P. The slight reduction in the intensity of XRD peaks of 1$RuCr_2O_3$-M is due to the incorporation of Ru on the surface of Cr_2O_3 to cause structural disorder during the reduction of noble metal ions by $NaBH_4$.[20] Compared with 1$RuCr_2O_3$-P, the interaction between Ru and Cr_2O_3-M is more intense to make the structure of 1$RuCr_2O_3$-M change. A similar phenomenon occurred in Raman spectra of samples, as shown in Fig. 1(b). The peaks centered at 301 (E_g), 340 (E_g), 540 (A_{1g}), and 595 (E_g) cm^{-1} correspond to E_g symmetry and A_{1g} symmetry of Cr_2O_3.[18,19] Peak intensity decreases after Ru loading on Cr_2O_3-M. In general, defects and lattice strains can affect the position and intensity of Raman peaks.[21] Compared with 1$RuCr_2O_3$-P, the stronger intensities of Raman peaks for 1$RuCr_2O_3$-M were probably due to the presence of strong interactions between Ru and Cr_2O_3-M.[22]

Generally, the variation of lattice parameters and lattice distortion often results in a change in XRD and Raman peak intensity.[23,24] The peak intensity of Cr_2O_3-M or 1$RuCr_2O_3$-M is stronger than that of Cr_2O_3-P or 1$RuCr_2O_3$-P, indicating more defects and absorbed oxygen on Cr_2O_3-P and 1$RuCr_2O_3$-P compared with Cr_2O_3-M and 1$RuCr_2O_3$-M. The decreased peak intensity of XRD and Raman spectra for 1$RuCr_2O_3$-M verified the SMSIs between Ru and surface lattice O, which was considered to be advantageous in VOC oxidation.[25,26]

The isotherms of nitrogen adsorption–desorption and pore size distribution status are presented in Fig. S2,† where a typical III isotherm with H3 hysteresis indicates irregular mesoporous structure in the as-prepared catalysts (Fig. S2(a)†).[19] The pore size distribution was calculated by the BJH method to further observe the pore structure of the materials. As shown in Fig. S2(b),† the pore diameter of the samples all have a dominating structure <40 nm. The difference is that, with a load of Ru species, the pore volume and average pore size of Cr_2O_3-P both decreased while they remain unchanged for Cr_2O_3-M under the same treatment (Table 1). The probable reason is that Ru ions were anchored with lattice oxygen of Cr_2O_3-M in the

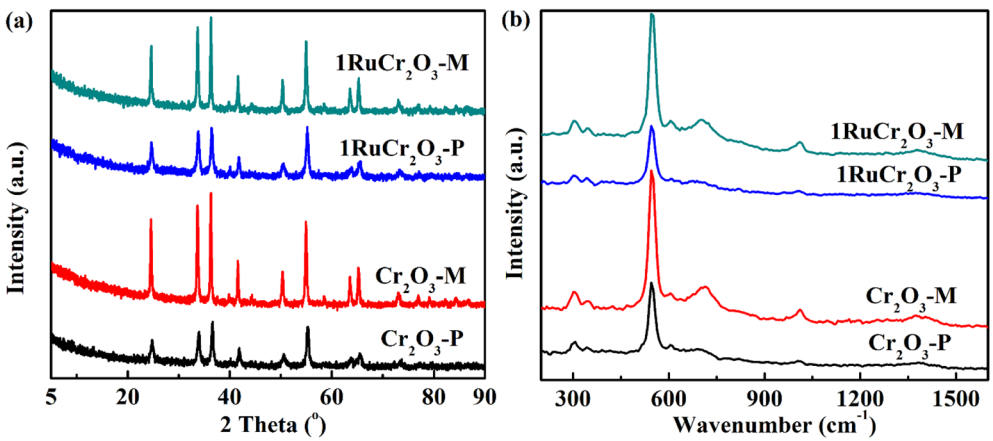

Fig. 1 XRD patterns (a) and Raman spectra (b) of catalysts.

Table 1 Nitrogen adsorption–desorption and XPS analysis of samples

Samples	BET (m^2 g^{-1})	Pore volume (m^3 g^{-1})	Average pore size (nm)	XPS (%)	
				Cr_2O_3/total (%)	O_{Sur}/O_{Latt} (%)
Cr_2O_3-P	34	0.4	47.9	38	70
Cr_2O_3-M	38	0.2	22.3	43	19
$1RuCr_2O_3$-P	31	0.3	39.2	44	18
$1RuCr_2O_3$-M	36	0.2	24.9	45	17

reduction process of $RuCl_3$ precursors and thus did not destroy the packing state of the Cr_2O_3 crystal. But for Cr_2O_3-P, the electrostatic interaction or packing state of the Cr_2O_3 crystal was broken after Ru was loaded on the surface of Cr_2O_3. This would lead to the rearrangement of grain crystals to be more tightly integrated. As a result, the pore volume and average pore size decreased accordingly.

3.2 Morphology characterization

To verify the results obtained by XRD and Raman, HRTEM, element mapping, and Cs-corrected STEM analysis were carried out to visually observe the distribution of noble metals. It can be seen in Fig. 2(a1 and b1) that the micro-morphology of $1RuCr_2O_3$-P and $1RuCr_2O_3$-M is similar to each other, showing irregular oval shapes. They have well-resolved lattice fringes with *d*-space values ~0.270 nm, which corresponds with the (104) crystal plane of Cr_2O_3. No noble metal nanoparticles (metallic Ru^0 or RuO_x) were observed on the surface with catalysts in HRTEM images of $1RuCr_2O_3$-P (a1) and $1RuCr_2O_3$-M (b1). However, the presence of precious metals was confirmed by the results of ICP-OES, element mapping characterizations (Fig. S3(a and b)†), and energy spectrum analysis (Fig. S1†). Therefore, it can be inferred that the supported Ru is too small to be observed at this scale and amplification.

To further investigate the interactions between Ru and Cr_2O_3 supports, a Cs-corrected HAADF-STEM analysis was conducted. It can be seen in Fig. 2(a2 and b2) that the simple reduction method possibly downsizes Ru into single atoms of less than 2 Angstrom (white dots on the surface of supports). There are also a few nanoclusters randomly anchored over the generally exposed low-index (104) facets of $1RuCr_2O_3$-P (Fig. 2(a3)).[27,28] By contrast, it can be seen that the single-atom Ru are arranged to anchor over the high index (223) facets of $1RuCr_2O_3$-M (Fig. 2(b3)). Theoretically, high-index faceted metal oxide has more edges, steps, or kinks, which expose a high density of low-coordinated atoms and can provide more active sites to take part in chemical reactions.[29] Also, it is recognized that immobilizing single atoms on the high-index facets of supports plays a crucial role in the stability of SACs with metal–support interactions.[30] Therefore, the good performance in the activity evaluation (Fig. 6) and durability tests (Fig. 7) under dry and humid conditions is probably due to the atomically dispersed Ru being anchored over the high-index facets, which offers more active sites for oxidation reactions.[31]

3.3 Surface physicochemical properties

To evaluate the surface element compositions of catalysts, XPS measurements were conducted. As shown in Fig. 3(a), the XPS

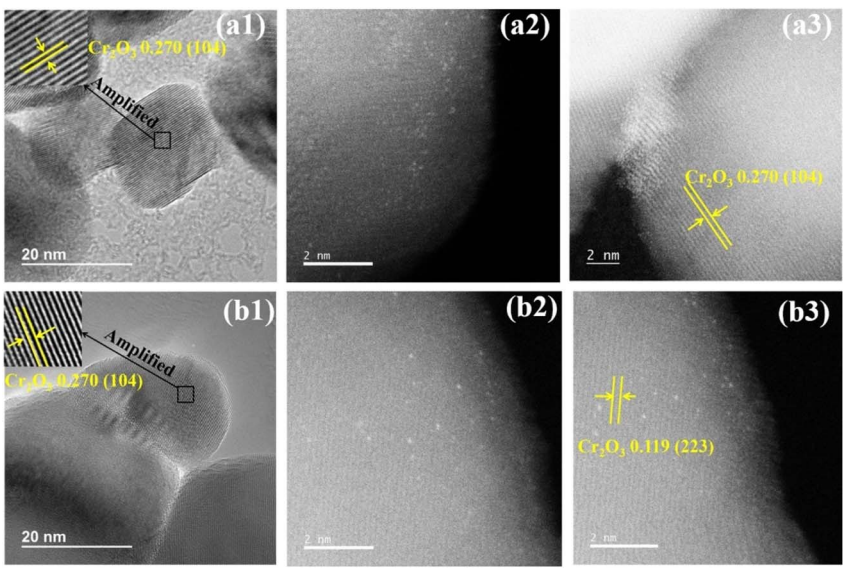

Fig. 2 HRTEM and Cs-corrected STEM images of samples: HRTEM (a1), Cs-corrected STEM (a2 and a3) images of $1RuCr_2O_3$-P; HRTEM (b1) and Cs-corrected STEM (b2 and b3) images of $1RuCr_2O_3$-M.

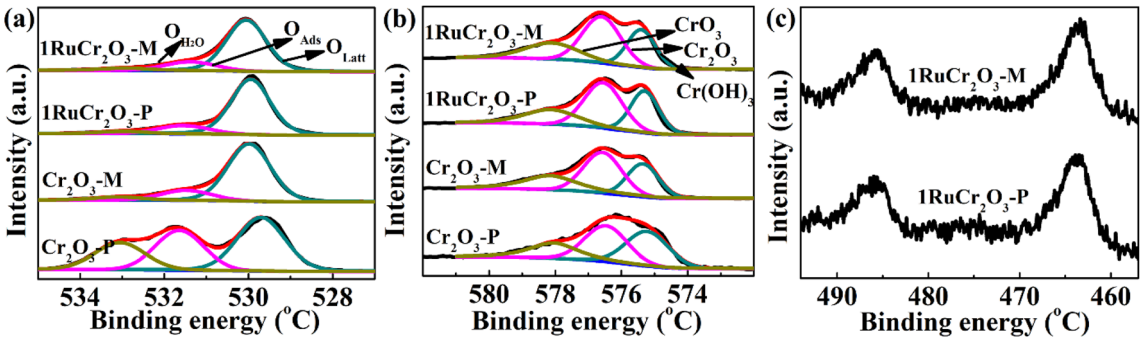

Fig. 3 XPS spectra of catalysts: O 1s (a), Cr $2p_{3/2}$ (b), Ru 3p (c).

spectra of O 1s were divided into three sections, where the first peak with binding energies ranging from 529.6 to 530.0 eV is ascribed to lattice oxygen (O_{Latt});[32,33] the second section in the 531.3–531.7 eV range is attributed to oxygen contained in defective sites, which is so-called adsorbed oxygen (O_{Ads});[34,35] and the minimum peak of the O 1s spectra centered at 533.0 eV could be identified as surface absorbed O_2 or H_2O.[36,37] The binding energy of lattice oxygen for Cr_2O_3-P is lower than that of the other three catalysts. That is because the excessive adsorbed oxygen in Cr_2O_3-P (~70% for the proportion of O_{Ads}/O_{Latt} as shown in Table 1) leads to the increased electron cloud densities of outer electrons in lattice oxygen. From Table 1, it can also be found that the ratio of O_{Ads}/O_{Latt} for $1RuCr_2O_3$-P (18%) is much lower than that for Cr_2O_3-P (70%), which could be attributed to the combination of Ru with absorbed oxygen of Cr_2O_3-P. And the slight decrease of absorbed oxygen in $1RuCr_2O_3$-M after Ru loading (from 19% to 17%) indicates that most Ru was anchored with lattice oxygen of Cr_2O_3-M. It could be concluded that the binding energy of oxygen species could be the critical factor for the combination of Ru with CrO_x support.

The Cr $2p_{3/2}$ XPS spectra were separated into three peaks with binding energies at about 575.4, 576.5, and 578.1 eV (Fig. 3(b)). The former peak can be attributed to $Cr(OH)_3$ species; the second is assigned to Cr_2O_3; and the peak centered at a high binding energy of 578.1 eV implies the existence of CrO_3 species.[38–40] Proportions of surface Cr are summarized in Table 1. This shows that the molar ratio of Cr_2O_3 species in catalyst Cr_2O_3-P is lower than that of Cr_2O_3-M, which could be attributed to more adsorbed oxygen and more defects in Cr_2O_3-P than in Cr_2O_3-M. The active adsorbed oxygen of Cr_2O_3-P laid the foundation for Ru to be combined with it. Therefore, the contents of Cr_2O_3 species in $1RuCr_2O_3$-P increased from 38% to 44% due to the combination of adsorbed oxygen species with Ru. The amounts of Cr_2O_3 species in $1RuCr_2O_3$-M were relatively unchanged. All the above analyses indicate that Ru is anchored with absorbed oxygen of $1RuCr_2O_3$-P and with lattice oxygen of $1RuCr_2O_3$-M, which could have various impacts on the catalytic efficiency for CB oxidation. The XPS curves of Ru 3p are shown in Fig. 3(c) for both supported catalysts. The binding energies at 486.0 and 463.0 eV are assigned to Ru $3p_{1/2}$ and Ru $3p_{3/2}$ electron orbit, respectively, which are associated with RuO_2 species.[41]

The reduction capacity and active oxygen desorption ability are the most important indicators of catalysts for catalytic oxidation of VOCs,[42,43] and are evaluated by characterizations of H_2-TPR and O_2-TPD, respectively. As shown in Fig. 4(a), the temperatures range from 170 to 370 °C which implies the reduction of Cr^{6+} to Cr^{3+}.[44–46] It can be seen that the initial reduction temperature of Cr_2O_3-P is a little higher than that of Cr_2O_3-M, and the reduction temperature range of Cr^{6+} to Cr^{3+} for Cr_2O_3-P is broader than that for Cr_2O_3-M. This suggests that Cr_2O_3-M is easier to be reduced and would perform better in CB oxidation. For supported Ru catalysts, the former two peaks at 100–170 °C are assigned to the reduction of RuO_2 to metallic Ru (Ru^0).[47,48] More specifically, the two peaks in the temperature range of 100–170 °C are attributed to the reduction of bulk oxygen of RuO_2 with H_2.[49] For $1RuCr_2O_3$-M, the RuO_2 is difficult to reduce compared with that in $1RuCr_2O_3$-P. It could be rationalized that Ru is anchored into lattice oxygen of $1RuCr_2O_3$-M due to a huge lattice matching, which resulted in a strong mental–support interaction (SMSI) of Ru with lattice oxygen. Previous studies indicated that strong interaction between atomically dispersed or other forms of noble metals and catalyst support makes the noble metals harder to reduce.[50,51] The reduction peaks of $1RuCr_2O_3$-M for Cr^{6+} to Cr^{3+} (170–370 °C) almost vanished after Ru application but were different with Cr_2O_3-P and $1RuCr_2O_3$-P. This implies that the combination of Ru and oxygen in $1RuCr_2O_3$-P does not have an impact on the reduction of Cr_2O_3-P support. It is different from the H_2-TPR analysis of $1RuCr_2O_3$-M, as there is nearly no reduction peak of Cr^{6+} to Cr^{3+}. The phenomenon implies the lattice oxygen species of Cr_2O_3-M is difficult to be moved during this temperature range. Corresponding to Cs-corrected STEM results, the H_2-TPR confirmed the different combination forms between single-atom Ru and oxygen species, where adsorbed oxygen and lattice oxygen are the main components to be anchored with Ru for $1RuCr_2O_3$-P and $1RuCr_2O_3$-M.

O_2-TPD is shown in Fig. 4(b), and it can be seen that there is much more adsorbed oxygen in Cr_2O_3-P in comparison with Cr_2O_3-M. The result is consistent with the analysis of XPS. In the spectrum of $1RuCr_2O_3$-P, a strong peak can be observed at a temperature of 680 °C, which indicates the desorption of bulk lattice oxygen. But for $1RuCr_2O_3$-M, nearly no peak can be observed from 70 to 800 °C, which further indicated the

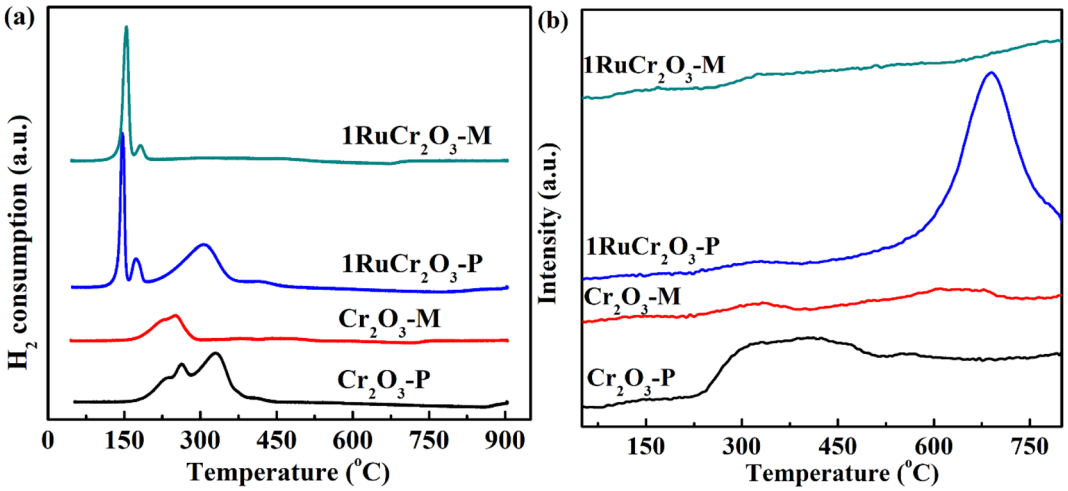

Fig. 4 H_2-TPR (a) and O_2-TPD (b) analysis of catalysts.

conclusion derived from Raman, XPS, and H_2-TPR of the SMSI between Ru and lattice oxygen of $1RuCr_2O_3$-M.

Acid site was considered as a crucial factor on catalyst activity and selectivity for heterogeneous catalysis.[52,53] NH_3-TPD was performed to study the acid sites of catalysts, and the profiles are shown in Fig. 5. The peak area and temperature location correspond to the amounts and varieties of acid sites on the surface of catalysts.[54] Brønsted acid sites are weaker than Lewis acids on the surface of Cr_2O_3, thus it is easier for NH_3 adsorbed on Brønsted acid sites to be released at a lower temperature than that on Lewis acid sites. And based on the intensities of acid sites, desorption peaks ranging from 100 to 350 °C could be attributed to the weak and medium acid sites, and desorption peaks at a higher temperature of ~600 °C imply strong acid sites.[55] So, peaks with temperatures below 200 °C (section I) could be ascribed to the desorption of physically adsorbed NH_3 and NH_4^+ on the weak Brønsted acid sites of catalysts. Section II between 230 and 470 °C indicates the desorption of NH_3 from strong Brønsted acid sites. Then, the desorption peaks contained in section III denote NH_3 is adsorbed on Lewis acid sites on the surface of catalysts. It can be inferred from the NH_3-TPD profiles that the contents of Brønsted acid sites on Cr_2O_3-M and $1RuCr_2O_3$-M are much larger than that on the surface of Cr_2O_3-P and $1RuCr_2O_3$-P. Based on previous reports,[56–58] the presence of Brønsted acid sites can result in nucleophilic substitution among chlorinated organics and acid sites, thereby degrading CB into phenolates and leading to ring cleavage. So, the catalysts with plenty of Brønsted acid sites (Cr_2O_3-M and $1RuCr_2O_3$-M) were considered beneficial to CB adsorption. Another point worth noting is that after Ru is supported on the catalysts, there is little difference in the Brønsted acid sites between Cr_2O_3-M and $1RuCr_2O_3$-M but with an obvious increase for $1RuCr_2O_3$-P compared with Cr_2O_3-P. The results indicate that the contents of Brønsted acid sites can be increased due to the supported Ru on the surface of catalysts ($1RuCr_2O_3$-P). If constrained to the lattice of support (Cr_2O_3-M), it would have little effect on the acid sites.

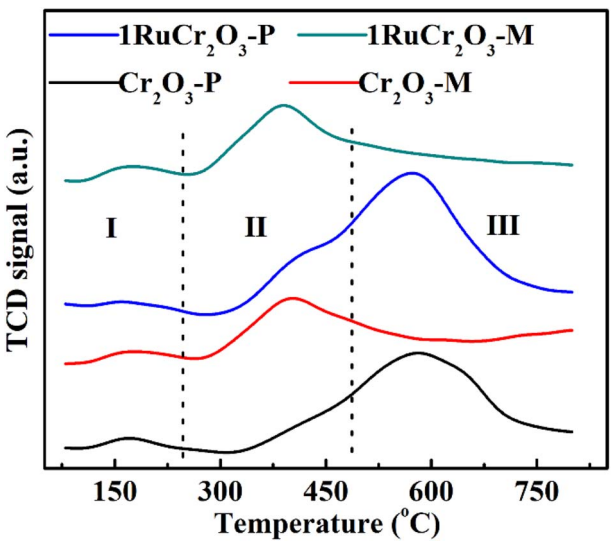

Fig. 5 NH_3-TPD profiles of catalysts.

3.4 Activity and durability tests

CB conversions and CO_2 mineralization rate of as-prepared catalysts with 120 000 mL (g^{-1} h^{-1}) of SV are shown in Fig. 6. As shown in Fig. 6, both CB conversion and CO_2 mineralization rate of Cr_2O_3-M are higher than that of Cr_2O_3-P, which is due to the higher BET surface area of Cr_2O_3-M. When the temperature is less than 260 °C, the conversion and CO_2 mineralization rate of $1RuCr_2O_3$-P is close to that of Cr_2O_3-M. That can be attributed to the better active oxygen desorption ability of Cr_2O_3-M at low temperatures (shown in Fig. 4(b)), and the surface oxygen of $1RuCr_2O_3$-P could be anchored by the Ru^{4+} and therefore not vulnerable to migrate at low temperature. When the temperature increases, the oxygen could be released from RuO_2 due to the redox reaction between CB and catalysts, which results in the increased activities of $1RuCr_2O_3$-P in high-temperature regions. But for $1RuCr_2O_3$-M, the CO_2 mineralization and CB

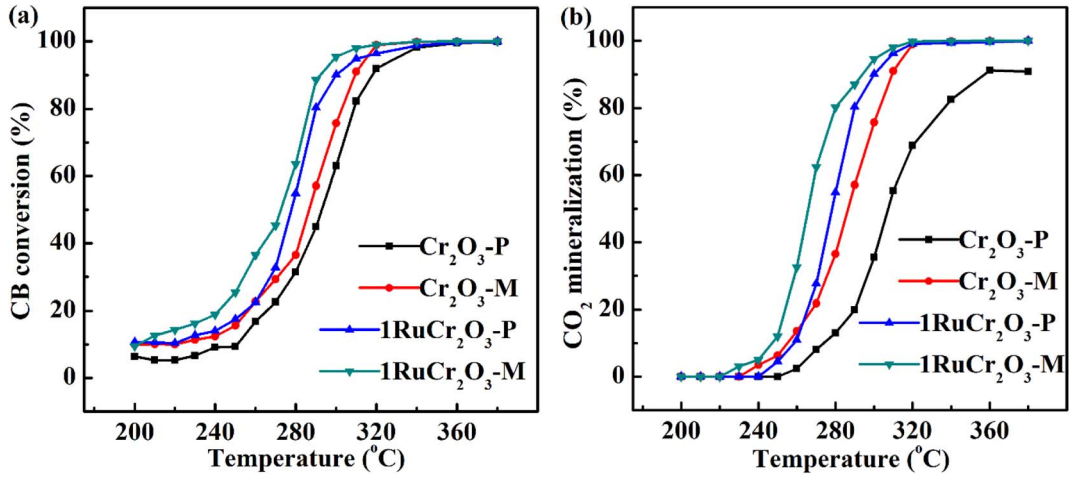

Fig. 6 CB conversion (a) and CO_2 mineralization rate (b) of the catalysts with CB concentration = 1000 ppm and SV = 120 000 mL (g^{-1} h^{-1}).

conversion is always higher than that of the other three catalysts with an increase in temperature. The result indicates that the active oxygen of $1RuCr_2O_3$-M works from low temperature to high temperature, unlike $1RuCr_2O_3$-M. From the activity performance above, it is reasonable to infer that the active oxygen of $1RuCr_2O_3$-M could be different with $1RuCr_2O_3$-P.

Because the turning points of temperature are located at ~300 °C for CB conversion and CO_2 mineralization rate of $1RuCr_2O_3$-P, the stability measurements were conducted at this temperature to further verify the above conclusion derived from activity tests under both dry and humid conditions. It can be seen from Fig. 7 that CB conversion and CO_2 mineralization rate of $1RuCr_2O_3$-P are lower than that of $1RuCr_2O_3$-M under dry conditions. With longer times, the CO_2 mineralization rate of $1RuCr_2O_3$-P declines more than that of $1RuCr_2O_3$-M. The phenomenon shown in the on-stream tests corresponds to the activities in Fig. 6. Moreover, it can be seen from the durability test under the humid condition that the conversion and mineralization rate of $1RuCr_2O_3$-M decreased due to the competitive adsorption of water vapor and CB. The CB conversion and CO_2 mineralization rate of $1RuCr_2O_3$-M are close to each other under humid conditions but have an obvious difference in dry conditions with a much higher conversion than mineralization rate, indicating the hydroxyl oxygen derived from water promoted the oxidation of CB.[59,60] Generally, the state of the noble metals could be crucial for the catalytic property in durability test. To observe the morphology and thoroughly comprehend the stability of $1RuCr_2O_3$-M, the used catalysts in dry and humid conditions were characterized by HRTEM and Cs-corrected STEM shown in Fig. S4.† It is interesting that after careful observation nano-sized or aggregated Ru could not be found using HRTEM. And Cs-corrected STEM confirmed the maintaining of single-atom Ru on the surface of $1RuCr_2O_3$-M. The result indicates that the as-prepared catalyst has the good thermal stability and crystal structure in long time high temperature process.

Based on the performance of catalysts and several characterizations, such as Cs-corrected STEM, O_2-TPD, H_2-TPR, and

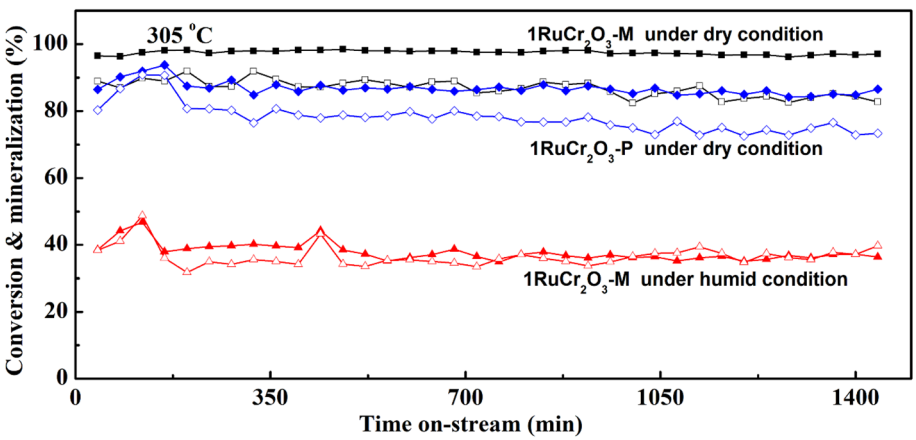

Fig. 7 Durability tests of $1RuCr_2O_3$-M under dry (black lines), humid conditions (relative humidity of 5%, red lines) and $1RuCr_2O_3$-P under dry condition (blue lines) at 305 °C with CB concentration = 1000 ppm and SV = 120 000 mL (g^{-1} h^{-1}), where the solid symbols represent CB conversion and hollow symbols denote CO_2 mineralization rate correspondingly.

XPS, it can be concluded that the binding form of Ru and oxygen species (adsorbed or lattice oxygen) could be the main factor for the durability of CB combustion. With similar Ru content and the same supports, the high tolerance of 1RuCr$_2$O$_3$-M on CB oxidation could be due to the SMSI between single-atom Ru and lattice oxygen (which makes CB deeply oxidized and suppresses the organochlorine adsorptions and coke accumulations).

4 Mechanism analysis

The CB adsorption and reaction pathway over the optimum catalyst (1RuCr$_2$O$_3$-M) were analyzed by *in situ* FT-IR measurements under different atmospheric pressures where 99.999% of N_2 was used to study the effect of lattice oxygen in CB oxidation at different temperatures. The reactions were examined at temperatures from 200 to 400 °C. Fig. 8(a) shows the CB adsorbed on the 1RuCr$_2$O$_3$-M catalyst as a function of temperature under the N_2 atmosphere. Several peaks identified at approximate 1582, 1478, and 1448 cm^{-1} are ascribed to the vibrations of ν(C=C), ν(C–H), and δ(C–H)/ν(C=C),[61] respectively, indicating adsorption of CB on the catalyst. The wavebands of 3000–4000 cm^{-1} are assigned as hydroxyl regions, where the peaks at 3638 and 3658 cm^{-1} imply the –OH being grafted on the Cr_2O_3 surface,[58] and the peaks at ~3730 and 2300 cm^{-1} originate from the produced H_2O and CO_2 at a temperature of 200 °C. Another peak at about 3420 cm^{-1} could also be identified as hydroxyl at the metal oxide surface. With increasing temperature, the reverse IR band at 3420 cm^{-1} indicated the consumption of –OH groups because of adsorption of CB. When the temperature was >200 °C, the produced H_2O and CO_2 almost disappeared, indicating the reaction was inhibited without air supply. The results indicated that the produced H_2O and CO_2 at the beginning were derived from the reaction products of surface lattice oxygen and CB. In the region of 1200–1700 cm^{-1}, peaks at ~1215, 1325 and 1394, 1657 cm^{-1} can be attributed to C–O stretching of surface phenolate,[56] surface carboxylates,[61] and C=O vibration of benzoquinone species,[58,62] respectively.

As shown in Fig. 8(b), air was introduced into the system. Some bands are observed at 1368, 1429, and 1891 cm^{-1} which can be assigned to chlorinated acetates, surface maleate species, and aldehyde-type species,[56,58,63] respectively. Another difference is that the bands corresponding to CO_2 (2350 cm^{-1}) and H_2O (3730 cm^{-1}) were enhanced when the air was introduced into the reaction system. A comparison with Fig. 8(a) indicates that the introduction of air can accelerate intermediate products derived from the reaction between surface lattice oxygen and CB to be deeply degraded into CO_2 and H_2O.

To sum, it can be concluded that catalyst 1RuCr$_2$O$_3$-M can convert CB into non-toxic products. The possible pathway for combustion oxidation of CB over 1RuCr$_2$O$_3$-M could be that CB was first adsorbed on the surface lattice oxygen of the catalyst to form surface phenolate species, which led to the change of electronic properties of the benzene ring. Then the benzoquinone-type species and some further oxidation products, including chlorinated acetates and surface maleate species, were observed due to the electrophilic substitution between the oxygen-containing group and chlorine substituents at a lower temperature. With the increase in temperature, the chlorinated acetates were transformed into aldehyde-type

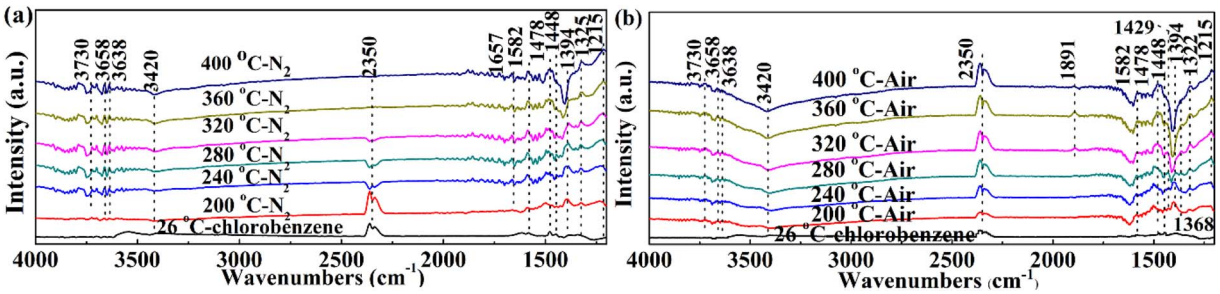

Fig. 8 *In situ* FT-IR analysis on 1RuCr$_2$O$_3$-M under exposure to chlorobenzene in N_2 (a) and high pure air (b).

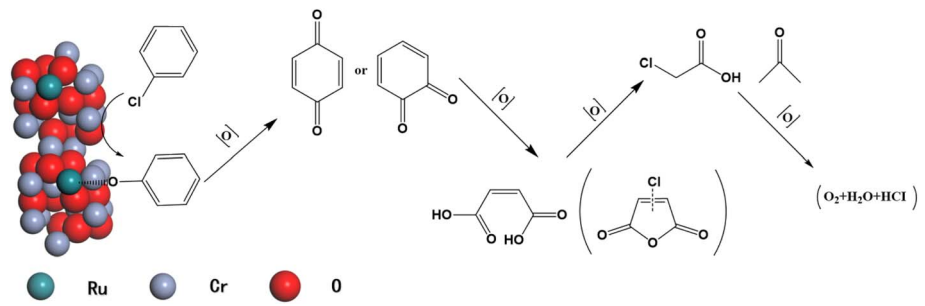

Fig. 9 The pathway of CB degradation over 1RuCr$_2$O$_3$-M.

species and finally formed CO_2, H_2O, and HCl. The detailed reaction pathway may proceed as the diagram shown in Fig. 9.

5 Conclusions

The Ru single-atom catalysts (Ru/Cr_2O_3) were successfully synthesized through a relatively simple reduction method for the efficient oxidation of CB—this is novel research for the preparation of SACs. The same metal oxides (Cr_2O_3) with different preparation methods resulted in different bonding between the noble metal Ru and supports Cr_2O_3, with Ru supported on the surface of Cr_2O_3-P while being confined in the lattice of Cr_2O_3-M. The results were related to the predominant oxygen species of catalyst supports, indicated by the characterizations of XPS and H_2-TPR. Due to the atomically dispersed Ru and its strong interaction (SMSI) with lattice oxygen of high-index facets of Cr_2O_3-M, the catalyst $1RuCr_2O_3$-M not only led to an excellent catalytic efficiency but also ensured durability and an anti-poisoning effect for CB oxidation. The study provides a simple and reliable way for the preparation of Ru-based SACs with SMSI. The good durability in chlorobenzene oxidation implies its practical potential application in this field, and the synthetic approach could be extended to other noble-metal catalysts.

Conflicts of interest

There are no conflicts to declare.

Acknowledgements

This work was supported by the Fundamental Research Program of Youth of Shanxi Province (No. 20210302124478, 20210302124347) and the Scientific and Technological Project of Shanxi Province (No. 201903D321082).

References

1 Y. Su, K. Fu, C. Pang, Y. Zheng, C. Song, N. Ji, D. Ma, X. Lu, C. Liu, R. Han and Q. Liu, *Environ. Sci. Technol.*, 2022, **56**, 9854–9871.
2 Y. Kuang and H. Li, *Renewable Sustainable Energy Rev.*, 2021, **151**, 111582.
3 H. Xu and H. Li, *J. Energy Chem.*, 2022, **73**, 133–159.
4 Y. Huang, S. Fang, M. Tian, Z. Jiang, Y. Wu and C. He, *Processes*, 2021, **9**, 19.
5 T. K. Nevanpera, S. Pitkaaho, S. Ojala and R. L. Keiski, *Molecules*, 2020, **25**, 4644.
6 G. Gan, S. Fan, X. Li, Z. Zhang and Z. Hao, *J. Environ. Sci.*, 2023, **123**, 96–115.
7 X. Lv, S. Cai, J. Chen, D. Yan, M. Jiang, J. Chen and H. Jia, *Catal. Sci. Technol.*, 2021, **11**, 4581–4595.
8 C. Li, Y. Zhao, H. Song and H. Li, *J. Chem. Technol. Biotechnol.*, 2020, **95**, 2069–2082.
9 Y. Su, K. Fu, Y. Zheng, N. Ji, C. Song, D. Ma, X. Lu, R. Han and Q. Liu, *Appl. Catal., B*, 2021, **288**, 119980.
10 H. Liu, X. Li, Q. Dai, H. Zhao, G. Chai, Y. Guo, Y. Guo, L. Wang and W. Zhan, *Appl. Catal., B*, 2021, **282**, 119577.
11 J. Jiang, W. Ding and H. Li, *Renewable Energy*, 2021, **179**, 1262–1270.
12 H. Liu, J. Yang, Y. Jia, Z. Wang, M. Jiang, K. Shen, H. Zhao, Y. Guo, Y. Guo, L. Wang, S. Dai and W. Zhan, *Environ. Sci. Technol.*, 2021, **55**, 10734–10743.
13 S. Lee, H. Han, W. Yoon and W. B. Kim, *Appl. Catal., A*, 2021, **611**, 117970.
14 M. Yoo, Y.-S. Yu, H. Ha, S. Lee, J.-S. Choi, S. Oh, E. Kang, H. Choi, H. An, K.-S. Lee, J. Y. Park, R. Celestre, M. A. Marcus, K. Nowrouzi, D. Taube, D. A. Shapiro, W. Jung, C. Kim and H. Y. Kim, *Energy Environ. Sci.*, 2020, **13**, 1231–1239.
15 Q. Kuang, X. Wang, Z. Jiang, Z. Xie and L. Zheng, *Acc. Chem. Res.*, 2014, **47**, 308–318.
16 J. Li, Z. Yang, Y. Li and G. Zhang, *J. Hazard. Mater.*, 2022, **429**, 128285.
17 Y. Huang, M. Tian, Z. Jiang, M. Ma, C. Chen, H. Xu, J. Zhang, R. Albilali and C. He, *Appl. Catal., B*, 2022, **304**, 121002.
18 X. Chen, X. Chen, S. Cai, J. Chen, W. Xu, H. Jia and J. Chen, *Chem. Eng. J.*, 2018, **334**, 768–779.
19 X. Chen, X. Chen, S. Cai, E. Yu, J. Chen and H. Jia, *Appl. Surf. Sci.*, 2019, **475**, 312–324.
20 P. S. Murphin Kumar, V. K. Ponnusamy, K. R. Deepthi, G. Kumar, A. Pugazhendhi, H. Abe, S. Thiripuranthagan, U. Pal and S. K. Krishnan, *J. Mater. Chem. A*, 2018, **6**, 23435–23444.
21 K. K. Mandari, J. Y. Do, A. K. R. Police and M. Kang, *Appl. Catal., B*, 2018, **231**, 137–150.
22 Z. Xi, D. P. Erdosy, A. Mendoza-Garcia, P. N. Duchesne, J. Li, M. Muzzio, Q. Li, P. Zhang and S. Sun, *Nano Lett.*, 2017, **17**, 2727–2731.
23 B. Li, L. Qiu and J. W. Tian, *J. Alloys Compd.*, 2018, **767**, 797–802.
24 W.-F. Chen, H. Chen, P. Koshy, A. Nakaruk and C. C. Sorrell, *Mater. Chem. Phys.*, 2018, **205**, 334–346.
25 X. Q. Yang, S. H. Liu, J. W. Li, J. Y. Chen and Z. B. Rui, *Chemosphere*, 2020, **249**, 1–8.
26 S. Akram, L. Chen, Q. Wang, X. R. Zhang, N. Han, G. L. Shen, Z. Wang and G. L. Ge, *Catal. Lett.*, 2017, **147**, 128–140.
27 W.-C. Huang, L.-M. Lyu, Y.-C. Yang and M. H. Huang, *J. Am. Chem. Soc.*, 2012, **134**, 1261–1267.
28 S. T. Hunt and Y. Román-Leshkov, *Acc. Chem. Res.*, 2018, **51**, 1054–1062.
29 C. X. Yang, Z. H. Li, H. L. Li, H. Liang, J. H. Liu, Y. C. Zhang, X. C. Wang, X. Y. Jiang, W. Z. Chen, J. Yuan, S. Q. Liu and X. Y. Li, *Sens. Actuators, B*, 2023, **374**, 132753.
30 X. Li, X. Yang, Y. Huang, T. Zhang and B. Liu, *Adv. Mater.*, 2019, **31**, 1902031.
31 S. Sun, X. Zhang, J. Cui, Q. Yang and S. Liang, *Nanoscale*, 2019, **11**, 15739–15762.
32 H.-J. Chun, Y. Lee, S. Kim, Y. Yoon, Y. Kim and S.-C. Park, *Appl. Surf. Sci.*, 2022, **578**, 152018.
33 G. Alba, M. P. Villar, R. Alcántara, J. Navas and D. Araujo, *Nanomaterials*, 2020, **10**, 1193.

34 S. Kozhukharov, C. Girginov, A. Tsanev and N. Boshkova, *Appl. Surf. Sci.*, 2022, **602**, 154254.
35 G. V. Prasath, K. S. Usha, M. Karuppaiah, G. Ravi and P. Krishnan, *J. Sol-Gel Sci. Technol.*, 2022, **104**, 198–210.
36 M. C. Biesinger, B. P. Payne, A. P. Grosvenor, L. W. M. Lau, A. R. Gerson and R. S. C. Smart, *Appl. Surf. Sci.*, 2011, **257**, 2717–2730.
37 W. Qin, L. Su, C. Yang, Y. Ma, H. Zhang and X. Chen, *J. Agric. Food Chem.*, 2014, **62**, 5827–5834.
38 W.-X. Zhang, Y. Liang, J.-W. Luo, A.-P. Jia, Y.-J. Wang, J.-Q. Lu and M.-F. Luo, *J. Mater. Sci.*, 2016, **51**, 6488–6496.
39 Y. Lin, W. Cai, X. Tian, X. Liu, G. Wang and C. Liang, *J. Mater. Chem.*, 2011, **21**, 991–997.
40 X.-Z. Fu, X.-X. Luo, J.-L. Luo, K. T. Chuang, A. R. Sanger and A. Krzywicki, *J. Power Sources*, 2011, **196**, 1036–1041.
41 Z. Mohamed, V. D. B. C. Dasireddy, S. Singh and H. B. Friedrich, *Int. J. Hydrogen Energy*, 2018, **43**, 22291–22302.
42 W. Si, Y. Wang, S. Zhao, F. Hu and J. Li, *Sci. Technol.*, 2016, **50**, 4572–4578.
43 Y. Wang, H. Arandiyan, J. Scott, M. Akia, H. Dai, J. Deng, K.-F. Aguey-Zinsou and R. Amal, *ACS Catal.*, 2016, **6**, 6935–6947.
44 J. S. B. Grzybowska, R. Grabowski, K. Wcisło, A. Kozłowska, J. Stoch and J. Zieliński, *J. Catal.*, 1998, **178**, 687–700.
45 G. Bai, H. Dai, Y. Liu, K. Ji, X. Li and S. Xie, *Catal. Commun.*, 2013, **36**, 43–47.
46 P. Xia, S. Zuo, F. Liu and C. Qi, *Catal. Commun.*, 2013, **41**, 91–95.
47 M. A. G. Hevia, A. P. Amrute, T. Schmidt and J. Pérez-Ramírez, *J. Catal.*, 2010, **276**, 141–151.
48 X. Liu, Q. Han, W. Shi, C. Zhang, E. Li and T. Zhu, *J. Catal.*, 2019, **369**, 482–492.
49 J. Shi, F. Hui, J. Yuan, Q. Yu, S. Mei, Q. Zhang, J. Li, W. Wang, J. Yang and J. Lu, *Catalysts*, 2019, **9**, 108.
50 Q. Zhang, X.-X. Qin, F.-P. Duan-Mu, H.-M. Ji, Z.-R. Shen, X.-P. Han and W.-B. Hu, *Angew. Chem., Int. Ed.*, 2018, **57**, 9351–9356.
51 Y. Luo, Q. Qian and Q. Chen, *Mater. Res. Bull.*, 2015, **62**, 65–70.
52 Y. Geng and H. Li, *Chemsuschem*, 2022, **15**, e202102495.
53 H. Wei, Z. Wang and H. Li, *Green Chem.*, 2022, **24**, 1930–1950.
54 M. Guo, Q. Liu, P. Zhao, J. Han, X. Li, Y. Ha, Z. Fu, C. Song, N. Ji, C. Liu, D. Ma and Z. Li, *Chem. Eng. J.*, 2019, **361**, 830–838.
55 H. Liu, L. Wei, R. Yue and Y. Chen, *Catal. Commun.*, 2010, **11**, 829–833.
56 J. Lichtenberger and M. D. Amiridis, *J. Catal.*, 2004, **223**, 296–308.
57 X. Weng, P. Sun, Y. Long, Q. Meng and Z. Wu, *Environ. Sci. Technol.*, 2017, **51**, 8057–8066.
58 J. Wang, X. Wang, X. Liu, T. Zhu, Y. Guo and H. Qi, *Catal. Today*, 2015, **241**, 92–99.
59 Y. Deng, S. Peng, H. Liu, S. Li and Y. Chen, *Front. Environ. Sci. Eng.*, 2019, **13**, 21.
60 P. Sun, W. Wang, X. Weng, X. Dai and Z. Wu, *Environ. Sci. Technol.*, 2018, **52**, 6438–6447.
61 Y. Liu, W. Wu, Y. Guan, P. Ying and C. Li, *Langmuir*, 2002, **18**, 6229–6232.
62 Y. Gu, T. Cai, X. Gao, H. Xia, W. Sun, J. Zhao, Q. Dai and X. Wang, *Appl. Catal., B*, 2019, **248**, 264–276.
63 G. Busca, G. Ramis and V. Lorenzelli, *J. Mol. Catal.*, 1989, **50**, 231–240.